Magnetic Proximity Effect and Anomalous Hall Effect in $Pt/Y_3Fe_{5-x}Al_xO_{12}$ Heterostructures

Xiao Liang,[1,2,4] Guoyi Shi,[3] Longjiang Deng,[1,4] Fei Huang,[1,4] Jun Qin,[1,4] Tingting Tang,[1,2] Chuangtang Wang,[1,4] Bo Peng,[1,4] Cheng Song,[3] and Lei Bi[1,4,*]

[1]*National Engineering Research Center of Electromagnetic Radiation Control Materials, University of Electronic Science and Technology of China, Chengdu 610054, China*

[2]*Information Materials and Device Applications Key Laboratory of Sichuan Provincial Universities, Chengdu University of Information Technology, Chengdu 610225, China*

[3]*Key Laboratory of Advanced Materials (MOE), School of Materials Science and Engineering, Tsinghua University, Beijing 100084, China*

[4]*State Key Laboratory of Electronic Thin-Films and Integrated Devices, University of Electronic Science and Technology of China, Chengdu 610054, China*

(Received 7 December 2017; revised manuscript received 4 July 2018; published 31 August 2018)

In this paper, we report an experimental and first-principles calculation study on the anomalous Hall effect (AHE) in $Pt/Y_3Fe_{5-x}Al_xO_{12}$ bilayer structures. Using a combinatorial pulsed-laser deposition method, we doped Al^{3+} ions in the $Y_3Fe_5O_{12}$ lattice with different concentrations, which preferentially substitute the tetrahedral Fe^{3+}, leading to significant variation of AHE. A monotonic decrease of anomalous Hall resistance R_{AHE} with increasing Al^{3+} doping concentration is observed at a temperature of 5 K, which scales linearly with the magnetic proximity effect- (MPE-)induced magnetic moments in Pt, as calculated using first-principles calculations. Temperature-dependent R_{AHE} characterizations indicate a sign change in R_{AHE} at around 100 K, which can be explained by a predominant contribution from spin Hall effect-(SHE-)induced AHE at higher temperatures. Our study demonstrates that the band hybridization and exchange coupling between tetrahedral Fe^{3+} ions and Pt are the major contributors to the magnetic proximity effect in Pt/YIG heterojunctions.

DOI: 10.1103/PhysRevApplied.10.024051

I. INTRODUCTION

$Pt/Y_3Fe_5O_{12}$(YIG) bilayer structures have been widely studied recently because they show rich physical phenomena caused by charge-magnon interaction at the heterojunction interface, such as spin pumping [1,2], spin Hall magnetoresistance (SMR) [3–6], spin Seebeck effect (SSE) [7–9], and anomalous Nernst effect (ANE) [8,9], etc. Physical interpretations of these phenomena can be generally attributed to spin Hall or interface magnetism mechanisms. These two mechanisms are under debate due to the unclear physical picture of the magnetic proximity effect (MPE) at the Pt/YIG interface [8–14], a phenomenon of ferromagnetic ordering of spins within several atomic layers of a noble metal (NM) film in close proximity to a ferromagnetic (FM) material. This interface magnetism in Pt has been characterized by x-ray magnetic circular dichroism (XMCD), a widely accepted method for element-specific characterization magnetic moments [15–18]. However, because the strength of MPE in Pt/YIG is very sensitive to the crystal structure at the Pt/YIG interface [19–22], different magnetic moments have been observed by various groups [15,16]. The anomalous Hall effect (AHE) is strongly related to the MPE. Depending on whether the MPE is present, the anomalous Hall resistance R_{AHE} in Pt is attributed to both the MPE and spin Hall effect (SHE), or pure SHE-induced R_{AHE} mechanisms, respectively. Several reports have focused on resolving the contribution of R_{AHE} from MPE and SHE at the Pt/YIG interface by angle-resolved resistance measurements [10,14,23–26], inserting an interface nonmagnetic Cu(Au) layer [10,25], and studying the temperature dependence of R_{AHE} [14,23,24]. These studies helped to clarify the origin of the AHE. However, the structural origin of the MPE and its quantitative relationship to R_{AHE} is still unclear.

In our previous work [27], using first-principles calculations, the hybridization between the interface tetrahedral Fe^{3+} 3*d* orbitals and the Pt 5*d* orbitals was observed to be the major contributor to the MPE, whereas the tetrahedral Fe^{3+} vacancies can significantly reduce the MPE-induced magnetic moment in Pt. In Al^{3+}-doped YIG thin films, the Al^{3+} ions preferentially occupy the tetrahedral sites [28], leading to nonmagnetic substitutions of the tetrahedral

*bilei00@gmail.com

Fe^{3+} ions, which may mimic the case of tetrahedral Fe vacancies. To prove the above considerations and to clarify the origin of MPE and AHE in Pt/YIG, in this work, we intentionally doped YIG with nonmagnetic Al^{3+}. By measuring the R_{AHE} in samples with different Al^{3+} doping concentrations and its temperature dependence, the quantitative relationship between R_{AHE} and the MPE-induced magnetic moment in Pt is studied. The results show that in Pt/YIG, the tetrahedral Fe^{3+} ions and its orbital hybridization with Pt are the major contributors to MPE and low-temperature AHE.

II. EXPERIMENTAL AND CALCULATION METHOD

$Y_3Fe_{5-x}Al_xO_{12}$ films are grown on gadolinium gallium garnet $Gd_3Ga_5O_{12}$ (GGG) (100) substrates by pulsed-laser deposition (PLD). A combinatorial deposition method with alternating laser pulses ablating on $Y_3Fe_5O_{12}$ and $Y_3Fe_{4.2}Al_{0.8}O_{12}$ ceramic targets is carried out to grow $Y_3Fe_{5-x}Al_xO_{12}$ thin films with different Al concentrations. The laser source is a Compex Pro 205 KrF laser operating at 248 nm. Prior to deposition, the chamber is pumped down to a base pressure of 5×10^{-7} mbar. The target-substrate distance is 5 cm. During deposition, the oxygen partial pressure P_{O2} is maintained at 0.13 mbar. The temperature of the substrates is kept at 800 °C. After deposition, P_{O2} is increased to 13 mbar to prevent oxygen-vacancy formation in $Y_3Fe_{5-x}Al_xO_{12}$. Samples are then maintained *in situ* at the deposition temperature for 10 min and then cooled down to room temperature with a cooling rate of −5 °C/min. All film thicknesses are kept around 150 nm. To accurately determine the Al ion concentrations, we dissolve the as-deposited $Y_3Fe_{5-x}Al_xO_{12}$ thin films in HNO_3 and measure their element compositions using inductively coupled plasma optical emission spectrometry (ICP OES) (SPECTRO ARCOS). The Al^{3+} ion concentration is determined as $x = 0$, 0.187, 0.392, 0.568, and 0.783 for different samples. The magnetic hysteresis loops of all samples are characterized on a superconducting quantum interference device (SQUID) at a temperature of 5 K. The $Y_3Fe_{5-x}Al_xO_{12}$ samples are transferred to a sputtering chamber for Pt deposition. Hall-bar-shaped Pt thin films with 7-nm thickness are subsequently deposited onto $Y_3Fe_{5-x}Al_xO_{12}$ thin films using magnetron sputtering through a shadow mask. The Hall resistance is then measured on a physical property measurement system (PPMS-9, Quantum Design). The source current is fixed to 1 mA for all characterizations.

A first-principles calculation method based on the density-functional theory (DFT) is carried out to evaluate the MPE at the Pt(100)/$Y_3Fe_{5-x}Al_xO_{12}$(100) interface. The Perdew-Burke-Ernzerhof (PBE) exchange-correlation function [29,30] and a plane-wave basis set within the framework of the projector augmented-wave (PAW) method [31,32] are employed. The k-point grids of the Monkhorst-Pack scheme are set to $(3 \times 3 \times 1)$ [33]. The DFT + U method is applied to correct the strong on-site Coulomb repulsion for the localized Fe ($3d$) states [34], and the effective value of U is set to 4.3 eV, which is widely used in other systems containing Fe^{3+} cations [35–37].

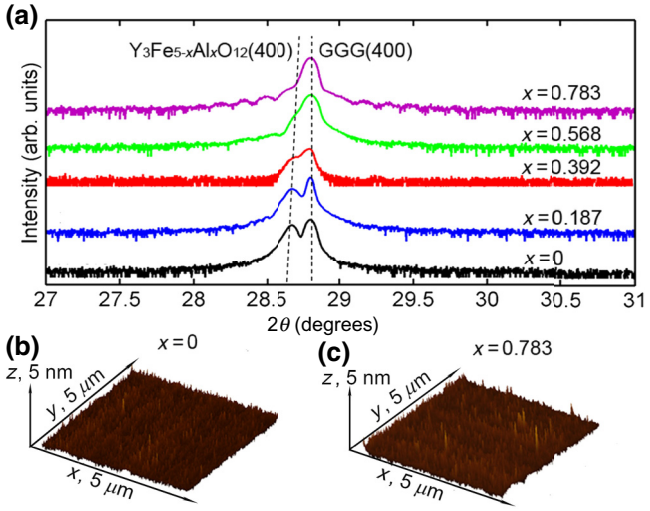

FIG. 1. (a) X-ray diffraction pattern of epitaxial $Y_3Fe_{5-x}Al_xO_{12}$ ($x = 0$, 0.187, 0.392, 0.568, 0.783) films grown on $Gd_3Ga_5O_{12}$ (GGG) (100) substrates. The surface morphology of (b) $Y_3Fe_5O_{12}$ and (c) $Y_3Fe_{4.217}Al_{0.783}O_{12}$ films in a 5×5 μm^2 area measured by atomic force microscopy.

III. RESULTS AND DISCUSSION

Figure 1(a) shows the XRD pattern of $Y_3Fe_{5-x}Al_xO_{12}$ thin films deposited on GGG(100) substrates. The (400) diffraction peaks of the GGG substrates are located at $2\theta = 28.80°$, whereas the film diffraction peak position shifts from 28.68° to higher 2θ angles with increasing Al^{3+} concentrations and eventually merges with the substrate peak. The decreased lattice constant in Al-doped YIG thin films is caused by the smaller ionic radius of Al^{3+} (50 pm) ions in oxygen tetrahedrons compared to Fe^{3+} (64 pm), which is consistent with previous reports [28]. Figures 1(b) and 1(c) show the surface morphology of the YIG and $Y_3Fe_{4.217}Al_{0.783}O_{12}$ thin films, respectively, measured by AFM. The root-mean-square roughnesses of all $Y_3Fe_{5-x}Al_xO_{12}$ thin films are 0.32 nm ($x = 0$), 0.61 nm ($x = 0.187$), 0.57 nm ($x = 0.392$), 0.48 nm ($x = 0.568$), and 0.45 nm ($x = 0.783$), respectively, indicating very smooth surfaces in all samples.

Figure 2(a) shows the magnetic hysteresis loops of the $Y_3Fe_{5-x}Al_xO_{12}$ thin films measured at 5 K with magnetic field applied perpendicular to the film plane. The saturation magnetization M_s of 201 emu/cm^3 measured in pure YIG thin films at 5 K is about 30% larger than its 300-K M_s value of 140 emu/cm^3, which agrees well with previous

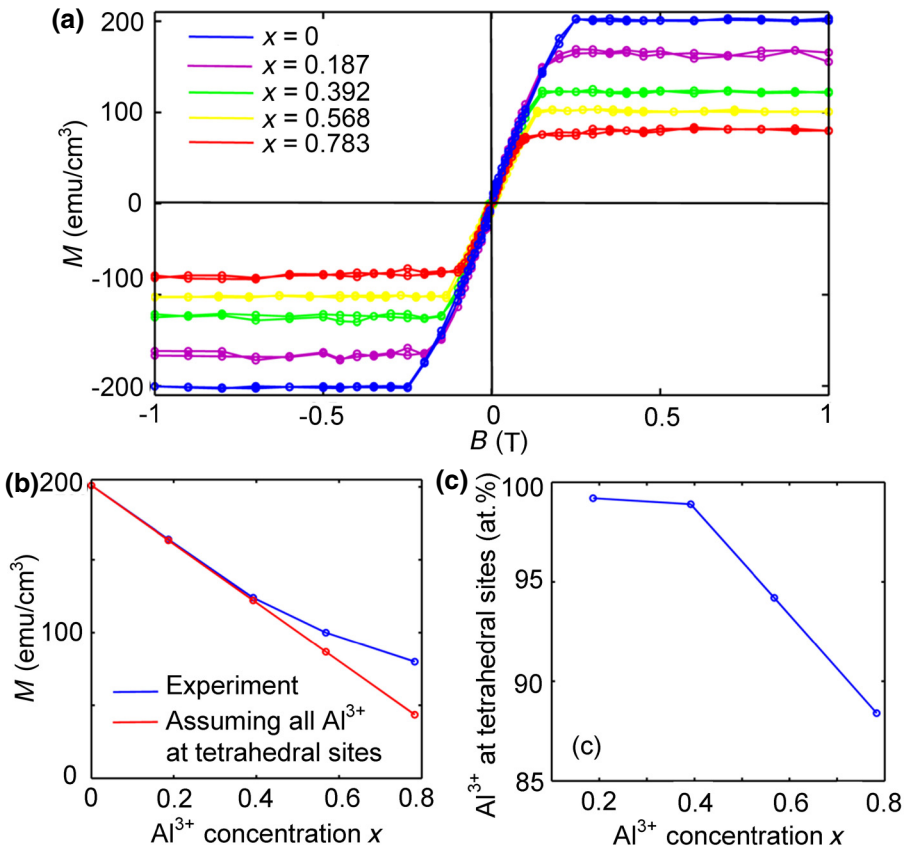

FIG. 2. (a) Out-of-plane magnetic hysteresis loops of $Y_3Fe_{5-x}Al_xO_{12}$ films measured at 5 K. (b) Comparison of saturation magnetization (M_s) of $Y_3Fe_{5-x}Al_xO_{12}$ films at 5 K through experimentally measured (blue line) and assuming Al^{3+} ions substitute the tetrahedral Fe^{3+} (red line). (c) The population of Al^{3+} ions occupying tetrahedral sites in $Y_3Fe_{5-x}Al_xO_{12}$.

studies [15]. The ferrimagnetism of a YIG unit cell is originated from 24 Fe^{3+} ions at the tetrahedral site antiferromagnetically coupled to the 16 Fe^{3+} ions at the octahedral site, leading to a net magnetic moment of 5 μ_B per unit cell. The saturation magnetization (M_s) of the Al-doped YIG films decreases with increasing Al^{3+} doping concentrations, indicating Al^{3+} ions mainly substitute the tetrahedral Fe^{3+}. Assuming that all nonmagnetic Al^{3+} ions substitute the tetrahedral Fe^{3+}, the M_s of $Y_3Fe_{5-x}Al_xO_{12}$ films should linearly decrease with increasing the Al^{3+} concentrations, as shown in Fig. 2(b) (red line). Our experimental results (blue line) show that the M_s of $Y_3Fe_{5-x}Al_xO_{12}$ films agree well with the above assumption with a doping concentration of $x \leq 0.392$. However, M_s becomes larger than the theoretical prediction with $x > 0.392$, indicating part of the Al^{3+} ions start to enter the octahedral sites. Although some Al^{3+} occupy octahedral sites in our $Y_3Fe_{5-x}Al_xO_{12}$ ($x = 0.568$, 0.783) films, the majority of Al^{3+} ions still occupy tetrahedral sites as revealed by the monotonic decrease of M_s by Al doping. The population of Al^{3+} occupying tetrahedral sites (y) and octahedral sites ($1 - y$) can be estimated using the following formula:

$$(3 - xy)m_{\mathrm{Fe}} - [2 - x(1 - y)]m_{\mathrm{Fe}} = M_s(x),$$

where m_{Fe} is the magnetization per unit volume of Fe^{3+} ions at 5 K. Using the $M_s(x = 0) = 201$ emu/cm^3, m_{Fe} can be determined as 201 emu/cm^3. Thus, the population of Al^{3+} occupying tetrahedral sites y can be obtained as shown in Fig. 2(c). One can see, 99.2, 98.9, 94.2, and 88.4 at.% out of all the Al^{3+} ions occupy tetrahedral sites in $Y_3Fe_{5-x}Al_xO_{12}$ ($x = 0.187$, 0.392, 0.568, 0.783) films, respectively.

Figure 3(a) shows the schematic diagram of the Hall measurements on our Pt/$Y_3Fe_{5-x}Al_xO_{12}$ devices at 5 K. A source current of 1 mA is applied along the x direction and the longitudinal voltage is measured by a nanovoltmeter along the y direction. Simultaneously, an external magnetic field ranging from 0.5 to −0.5 T is applied perpendicular to the film plane. The Hall resistance measured at 5 K shows a nonlinear relationship with the external magnetic field, as shown in Fig. 3(b), indicating that AHE is observed in all samples. Figure 3(c) shows the pure anomalous Hall resistance of Pt/$Y_3Fe_{5-x}Al_xO_{12}$ after subtracting the linear ordinary Hall resistance part. Because $Y_3Fe_{5-x}Al_xO_{12}$ is insulating for all Al concentrations, as confirmed by four-probe electrical-resistance characterizations, the R_{AHE} is exclusively from the Pt layer. The R_{AHE} monotonically decreases with increasing Al^{3+} concentrations, suggesting a reduced magnetic moment in Pt. Figure 3(d) shows the variations of R_{AHE} and M_s as a function of Al^{3+} ion populations in $Y_3Fe_{5-x}Al_xO_{12}$ in comparison with the free-doping case. It is found that R_{AHE} decreases much faster than M_s. For the maximum Al^{3+}

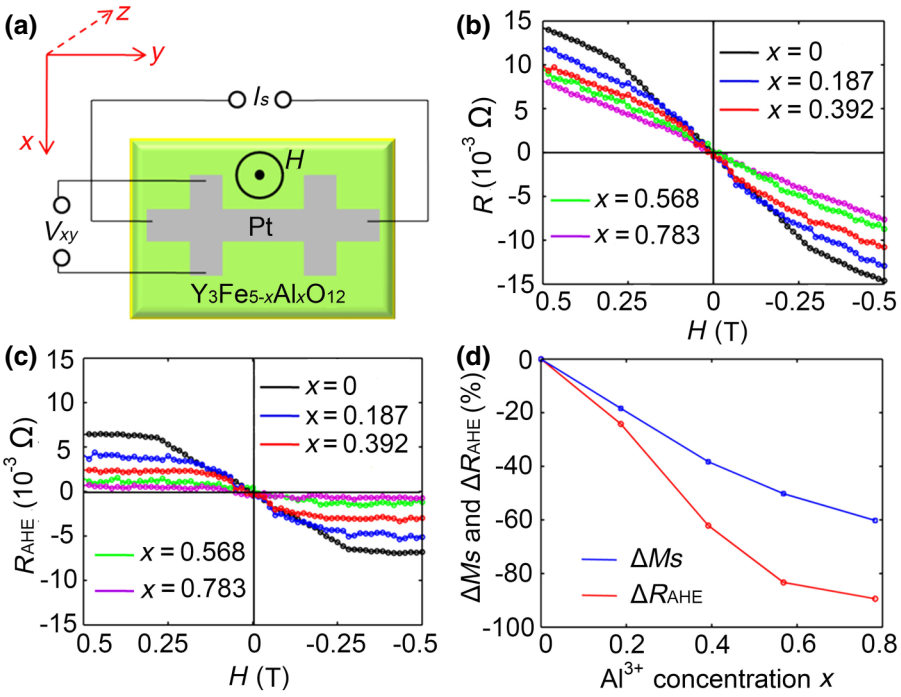

FIG. 3. (a) Schematic diagram of the Hall measurement set up. (b) The Hall resistance of $Pt/Y_3Fe_{5-x}Al_xO_{12}$ devices measured at 5 K by PPMS. (c) The anomalous Hall resistance (R_{AHE}) of $Pt/Y_3Fe_{5-x}Al_xO_{12}$ devices, where the linear ordinary Hall resistance part is subtracted. (d) Variations of the saturation magnetization of $Y_3Fe_{5-x}Al_xO_{12}$ films and saturation R_{AHE} of $Pt/Y_3Fe_{5-x}Al_xO_{12}$ devices in comparison with pure YIG systems.

ion concentrations of 0.783, M_s reduces to 60.2% of the Pt/YIG case, compared to a 89.4% reduction of the AHE signal. Such observations indicate that R_{AHE} is not linearly related to M_s of $Y_3Fe_{5-x}Al_xO_{12}$. Instead, the tetrahedral Fe population may play the critical role of the observed AHE.

To determine the origin of R_{AHE}, temperature dependence of R_{AHE} in Pt/YIG and $Pt/Y_3Fe_{4.8}Al_{0.2}O_{12}$ is characterized in Figs. 4(a) and 4(b), respectively. In both systems, the R_{AHE} firstly decreases with increasing temperature, then reaches 0 around 100 K, then increases with a negative sign with further increasing temperature up to room temperature. Similar R_{AHE}-T dependence in Pt/YIG has been reported by other researchers [10,23,38]. The Curie temperature of YIG is about 560 K and is above 400 K with Al doping ($x < 1$) [39,40]. There is no anomaly in the M-T curve both in YIG and Al : YIG around 100 K, therefore, the R_{AHE} sign changing around 100 K should be independent of YIG or Al : YIG magnetization. From previous studies, the R_{AHE} can be originated from two mechanisms: one is MPE, in which $R_{AHE} \propto M_z$ [41,42]; the other is SHE, in which $R_{AHE} \propto -M_z$ [4], where $M_z = Cm_z$ is the induced magnetization in Pt, m_z is the unit vector along the out-of-plane orientation of magnetization, and C is a constant. Meanwhile, the SHE in Pt/YIG shows lower amplitude with decreasing temperature from 100 K to lower temperatures, possibly due to a smaller spin Hall angle value at lower temperatures [43], whereas the MPE-induced magnetic moment in Pt increases with decreasing temperature [44]. Based on the above considerations and the experiment data, we may tentatively separate the physical origin of R_{AHE} into three temperature regions: In the low-temperature region (<20 K), R_{AHE} quickly decreases with increasing temperature, indicating a dominant MPE-induced AHE over SHE; in the intermediate temperature region (50–100 K), the two mechanisms caused R_{AHE} with similar amplitude but opposite signs. In addition, the total R_{AHE} approaches 0; in the high-temperature region, SHE is the dominant contributor to R_{AHE} and the net R_{AHE} shows an opposite sign to that at low temperatures. It should be noted that the sign change of R_{AHE} with temperature has also been interpreted as a sign change of the imaginary part of the spin-mixing conductance G_i or a sign change of MPE in previous reports [23,38]. This difference may be attributed to different Pt/YIG interface lattice structures of different samples. Nevertheless, a consensus of the increasing R_{AHE} with decreasing temperature at the low-temperature region should be dominated by MPE [14,24,25,42]. Figure 4(c) shows the saturated R_{AHE} in $Pt/Y_3Fe_5O_{12}$ and $Pt/Y_3Fe_{4.813}Al_{0.187}O_{12}$ devices at various temperatures. At low temperatures below 20 K, the R_{AHE} of $Pt/Y_3Fe_{4.813}Al_{0.187}O_{12}$ is smaller than that of $Pt/Y_3Fe_5O_{12}$ at the same temperature. In addition, R_{AHE} reaches 0 at a temperature lower than 100 K in $Pt/Y_3Fe_{4.813}Al_{0.187}O_{12}$, while it reaches 0 at a temperature higher than 100 K in $Pt/Y_3Fe_5O_{12}$. Therefore, Al^{3+} doping can decrease the MPE-induced R_{AHE} in Pt/YIG. To verify MPE and SHE contributions at different temperatures, the angle-resolved magnetoresistance MR_{xx} of the Pt/YIG sample at 10 and 300 K are measured, as shown in Fig. 4(d). During the measurement, the magnetic field is kept to 2 T and paralleled to the source current direction, and then rotated from in-plane to out-plane direction (x-z plane, see inset figure). It is clear that MR_{xx} is cosine dependent on the angle γ at 10 K; however, there

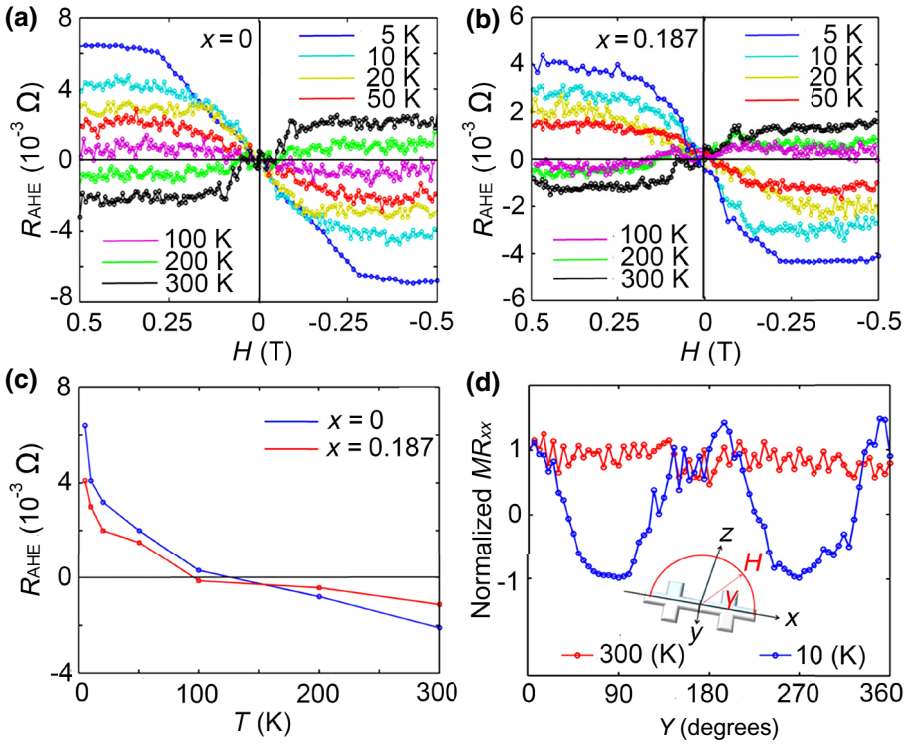

FIG. 4. (a),(b) Anomalous Hall resistance (R_{AHE}) of $Pt/Y_3Fe_5O_{12}$ and $Pt/Y_3Fe_{4.813}Al_{0.187}O_{12}$ devices measured at different temperatures, respectively. (c) Comparison of the saturated R_{AHE} in $Pt/Y_3Fe_5O_{12}$ and $Pt/Y_3Fe_{4.813}Al_{0.187}O_{12}$ devices at various temperatures.

is no dependence on γ at 300 K, which indicates AMR (originates from MPE) and SMR (originates from SHE), respectively [3]. Therefore, MPE and SHE is the dominant mechanism of interfacial interaction at low and high temperatures, which also reflect on the AHE differences.

The above argument is further supported by analyzing the relationship between R_{AHE} and R_0 at different temperatures, as shown in Fig. 5, where R_0 is the intrinsic resistance of the Pt Hall bar. In previous studies, it has been observed that R_{AHE} of the magnetic metal materials with high conductivity is proportional to R_0 and R_0^2 at low and high temperatures due to skew scattering and the side-jump mechanism, while the SHE-induced R_{AHE} is proportional to R_0^2 at any temperature [4,41]. In Fig. 5, both in $Pt/Y_3Fe_{4.813}Al_{0.187}O_{12}$ and $Pt/Y_3Fe_5O_{12}$, R_{AHE} is approximately linear dependent on R_0 when $T < 20$ K and has a quadratic relationship to R_0 when $T > 100$ K. Therefore, in $Pt/Y_3Fe_{5-x}Al_xO_{12}$, MPE is considered as the dominant contribution to R_{AHE} ($T < 20$ K). At high temperature, both MPE- and SHE-induced R_{AHE} can be proportional to R_0^2 and it is hard to distinguish MPE and SHE contributions. However, combining the experimental results of sign changing in R_{AHE} around 100 K, we can expect the SHE is the predominant factor, otherwise, R_{AHE} should still be a positive value at high temperature.

To verify that Al^{3+} doping of tetrahedral Fe^{3+} indeed influences the MPE, first-principles calculation is carried out to study the interface magnetism in $Pt/Y_3Fe_{5-x}Al_xO_{12}$. Figure 6(a) shows the calculation models of the $Pt(100)/Y_3Fe_{5-x}Al_xO_{12}(100)$ heterostructures. A 15-Å-thick vacuum layer is inserted to avoid the interaction between two cells. We first substitute one tetrahedron Fe^{3+} to Al^{3+} in one of the five termination layers Y1, Y2, Y3, Y4, and Y5, namely Al(Y1), Al(Y2), Al(Y3), Al(Y4), and Al(Y5), respectively. These cases correspond to an Al^{3+} dopant concentration of $x = 0.18$,

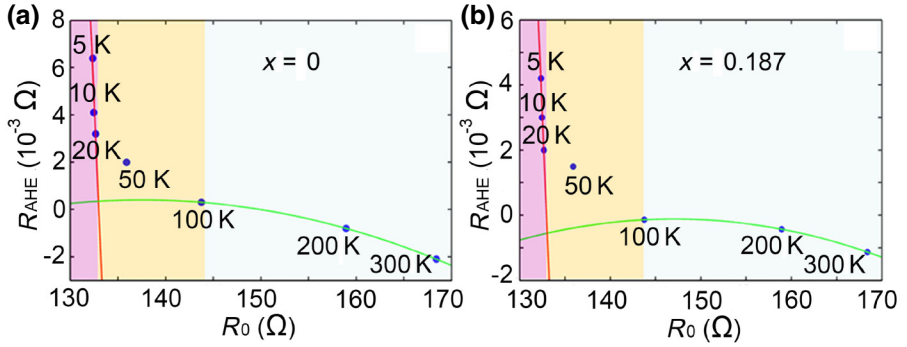

FIG. 5. R_{AHE} versus the intrinsic resistance of Pt Hall bars (R_0) in (a) $Pt/Y_3Fe_5O_{12}$ and (b) $Pt/Y_3Fe_{4.813}Al_{0.187}O_{12}$ at various temperatures. Red and green lines assume a linear and quadratic relationship between R_{AHE} and R_0, respectively.

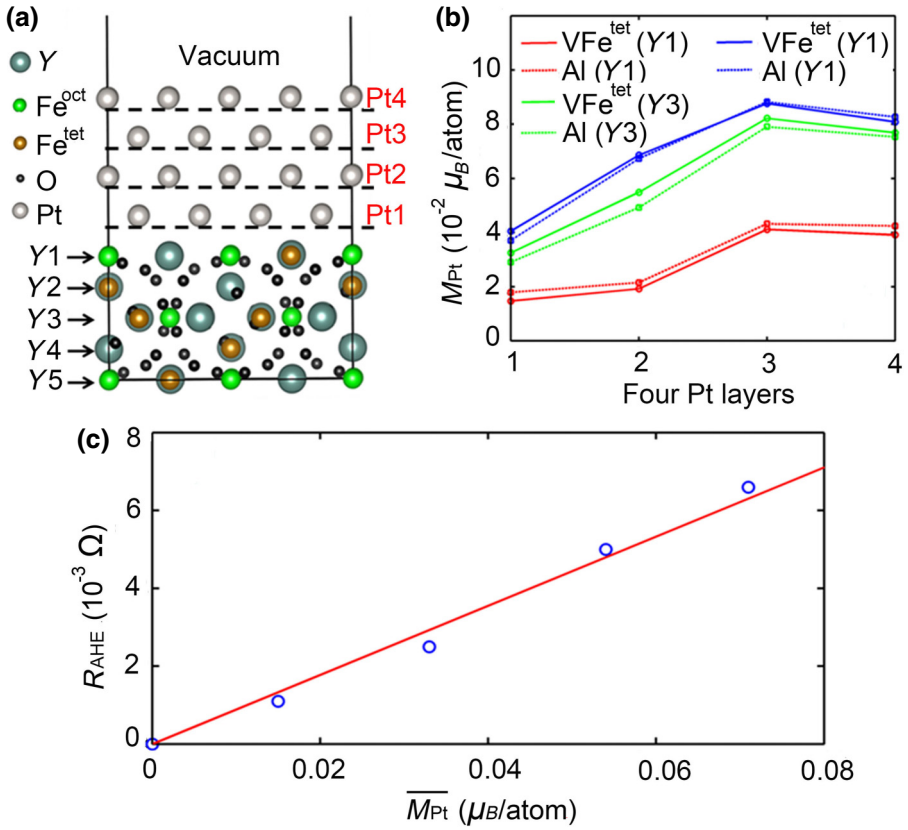

FIG. 6. (a) Schematic diagram of the Pt(100)/$Y_3Fe_{5-x}Al_xO_{12}$(100) unit cell. A 15-Å-thick vacuum layer is inserted to avoid the interaction between two cells. (b) The calculated average magnetic moment per Pt atom in each of the four Pt layers in Pt/YIG after introducing one Al^{3+} impurity (dashed line) or Fe^{3+} vacancy (solid line) at the same tetrahedron sites in YIG. (c) Experiment R_{AHE} versus the calculated average magnetic moment per Pt atom in Pt/$Y_3Fe_{5-x}Al_xO_{12}$(100) heterostructures.

which is closed to the experimental case of $x = 0.187$. We also made a comparison with the case where Al^{3+} ions are replaced by tetrahedral Fe vacancies. Figure 6(b) shows the average magnetic moments per Pt atom in each of the four Pt layers for the Al(Y1), Al(Y2), and Al(Y3) cases, respectively. Introducing Al^{3+} clearly decreases the MPE-induced magnetic moments in Pt, which is comparable to the case of introducing one tetrahedral Fe^{3+} vacancy at the same location. We extended this calculation to high Al^{3+} dopant concentrations. Table I shows the average magnetic moments (M_{Pt}) over all Pt atoms with different Al^{3+} doping concentration and locations. The Al concentrations are $x = 0$, 0.18, 0.36, and 0.54 (corresponding to 0, 1, 2, 3 Al^{3+} ions in each termination layer,

TABLE I. Calculated magnetic moments per Pt atom (M_{Pt}) in Pt/$Y_3Fe_{5-x}Al_xO_{12}$ with different Al^{3+} ion locations [see Fig. 5(a)]. ΔM is the variation in M_{Pt} compared with the $x = 0.0$ case. $\overline{M_{Pt}}$ and $\overline{\Delta M}$ are averaged overall different ion locations.

Al^{3+} Concentration	Location	M_{Pt} (μ_B)	ΔM	$\overline{M_{Pt}}$ (μ_B)	$\overline{\Delta M}$
$x = 0.0$	-	0.071	-	0.071	-
$x = 0.18$	Y1	0.031	−56.3%	0.054	−23.9%
	Y2	0.048	−32.4%		
	Y3	0.057	−19.7%		
	Y4	0.064	−9.8%		
	Y5	0.068	−4.2%		
$x = 0.36$	Y1	0.008	−88.7%	0.033	−53.5%
	Y2	0.018	−74.6%		
	Y3	0.032	−54.9%		
	Y4	0.043	−39.4%		
	Y5	0.062	−12.7%		
$x = 0.54$	Y1	−0.022	−131.0%	0.015	78.9%
	Y2	−0.007	−110.0%		
	Y3	0.017	−76.1%		
	Y4	0.031	−56.3%		
	Y5	0.058	−18.3%		

respectively), close to experiment values of $x = 0$, 0.187, 0.392, and 0.568, respectively. One can see the induced magnetism of Pt decreases more with the Al^{3+} ions moving closer to the $Pt/Y_3Al_xFe_{5-x}O_{12}$ interface. (We did not consider the influence of Al ions farther than five atomic layers from the Pt/YIG interface to MPE as they contribute 1 order less than the interface Al ions.) By assuming Al^{3+} ions are homogeneously distributed in YIG, they have the same probability to appear at any of the Y1–Y5 layers. Therefore, for a certain dopant concentration, we define $\overline{M_{Pt}}$ and $\overline{\Delta M}$ as the average value of M_{Pt} and ΔM over all Y1–Y5 cases, revealing the effect of a random distribution of Al^{3+} doping on MPE of Pt/YIG. We can see with increasing Al^{3+} concentrations, $\overline{M_{Pt}}$ decreases rapidly, leaving only 21.1% when $x = 0.54$ compared to the Al^{3+} dopant-free case. If R_{AHE} at 5 K, as shown in Fig. 3(b), is mainly due to the MPE of $Pt/Y_3Fe_{5-x}Al_xO_{12}$, we should have $R_{AHE}(\overline{M_{Pt}}) = \beta\overline{M_{Pt}}$ for the ferromagnetic Pt, where $\overline{M_{Pt}}$ is the average magnetization of Pt atoms and β is a magnetization-independent parameter [41,42]. We plot the measured R_{AHE} as a function of the calculated $\overline{M_{Pt}}$, as shown in Fig. 6(c). (Here we assume the Al concentrations are the same as the experiment values and Al only occupies the tetrahedral sites, which is generally true based on our experimental analysis.) Clearly, we observe a linear relationship between $\overline{M_{Pt}}$ and R_{AHE}, as shown by the linear-fitting red line. From the linear-fitting results, the parameter β can be solved to be 87.3 $m\Omega/\mu_B$, i.e., introducing 1 μ_B magnetic moment per atom to Pt by MPE can lead to 87.3 mΩ of R_{AHE}. The good linear fitting between and R_{AHE} further confirms the origin of R_{AHE} from MPE at low temperatures.

IV. CONCLUSION

In summary, AHE in $Pt/Y_3Fe_{5-x}Al_xO_{12}$ is studied in this paper. Al^{3+} ions preferentially substitute the tetrahedral Fe^{3+} ions, leading to reduced MPE and lower AHE. Compared to $Pt/Y_3Fe_5O_{12}$, the saturation anomalous Hall resistance R_{AHE} in $Pt/Y_3Fe_{5-x}Al_xO_{12}$ decreases by 24.2, 62.1, 83.3, and 89.4% with Al^{3+} doping concentrations of $x = 0$, 0.187, 0.392, 0.568, and 0.783 at 5 K, which shows a linear relationship with the magnetic proximity effect-induced magnetic moments in Pt as calculated using the first-principles calculation method, with a slope factorβ of 87.3 $m\Omega/\mu_B$. This proximity effect-induced R_{AHE} quickly decreases with increasing temperature in $Pt/Y_3Fe_{5-x}Al_xO_{12}$, leading to a dominant SHE-induced AHE at temperatures above 100 K. Our results demonstrate that tetrahedral Fe^{3+} ions are the main contributors to the MPE and AHE at $Pt/Y_3Fe_5O_{12}$ interfaces at low temperatures.

ACKNOWLEDGMENTS

We are grateful for the support of the National Natural Science Foundation of China (Grants No. 61475031 and No. 51522204), Ministry of Science and Technology of China (MOST No. 2016YFA0300802), the Fundamental Research Funds for the Central Universities (Grant No. ZYGX2014Z001), the Science Foundation for Youths of Sichuan Province (Grant No. 2015JQO014) and the Doctoral Fund of Ministry of Education of China (Grant No. 20130185120009).

X.L. and G.S. contributed equally to this work.

[1] Y. Y. Sun, H. Chang, M. Kabatek, Y. Song, Z. H. Wang, M. Jantz, W. Schneider, and M. Z. Wu, Damping in Yttrium Iron Garnet Nanoscale Films Capped by Platinum, Phys. Rev. Lett. **111**, 106601 (2013).

[2] H. L. Wang, C. H. Du, Y. Pu, R. Adur, P. C. Hammel, and F. Y. Yang, Scaling of Spin Hall Angle in 3d, 4d, and 5d Metals from $Y_3Fe_5O_{12}$/Metal Spin Pumping, Phys. Rev. Lett. **112**, 197201 (2014).

[3] H. Nakayama, M. Althammer, Y. T. Chen, K. Uchida, Y. Kajiwara, D. Kikuchi, T. Ohtani, S. Geprägs, M. Opel, S. Takahashi, R. Gross, G. E. W. Bauer, S. T. B. Goennenwein, and E. Saitoh, Spin Hall Magnetoresistance Induced by a Nonequilibrium Proximity Effect, Phys. Rev. Lett. **110**, 206601 (2013).

[4] Y. T. Chen, S. H. Nakayama, M. Althammer, S. T. B. Goennenwein, E. Saitoh, and G. E. W. Bauer, Theory of spin Hall magnetoresistance, Phys. Rev. B **87**, 144411 (2013).

[5] J. H. Han, C. Song, F. Li, Y. Y. Wang, G. Y. Wang, Q. H. Yang, and F. Pan, Antiferromagnet-controlled spin current transport in $SrMnO_3$/Pt hybrids, Phys. Rev. B **90**, 144431 (2014).

[6] J. H. Han, C. Song, S. Gao, Y. Wang, C. Chen, and F. Pan, Realization of the meminductor, ACS Nano **8**, 10043 (2014).

[7] D. Qu, S. Y. Huang, J. Hu, R. Wu, and C. L. Chien, Intrinsic Spin Seebeck Effect in Au/YIG, Phys. Rev. Lett. **110**, 067206 (2013).

[8] T. Kikkawa, K. Uchida, Y. Shiomi, Z. Qiu, D. Hou, D. Tian, H. Nakayama, X. F. Jin, and E. Saitoh, Longitudinal Spin Seebeck Effect Free from the Proximity Nernst Effect, Phys. Rev. Lett. **110**, 067207 (2013).

[9] T. Kikkawa, K. Uchida, S. Daimon, Y. Shiomi, H. Adachi, Z. Qiu, D. Hou, X. F. Jin, S. Maekawa, and E. Saitoh, Separation of longitudinal spin Seebeck effect from anomalous Nernst effect: Determination of origin of transverse thermoelectric voltage in metal/insulator junctions, Phys. Rev. B **88**, 214403 (2013).

[10] B. F. Miao, S. Y. Huang, D. Qu, and C. L. Chien, Physical Origins of the New Magnetoresistance in Pt/YIG, Phys. Rev. Lett. **112**, 236601 (2014).

[11] S. Y. Huang, W. G. Wang, S. F. Lee, J. Kwo, and C. L. Chien, Intrinsic Spin-Dependent Thermal Transport, Phys. Rev. Lett. **107**, 216604 (2011).

[12] S. Y. Huang, X. Fan, D. Qu, Y. P. Chen, W. G. Wang, J. Wu, T. Y. Chen, J. Q. Xiao, and C. L. Chien, Transport Magnetic

Proximity Effects in Platinum, Phys. Rev. Lett. **109**, 107204 (2012).
[13] V. L. Grigoryan, W. Guo, G. E. W. Bauer, and J. Xiao, Intrinsic magnetoresistance in metal films on ferromagnetic insulators, Phys. Rev. B **90**, 161412 (2014).
[14] T. Lin, C. Tang, H. M. Alyahayaei, and J. Shi, Experimental Investigation of the Nature of the Magnetoresistance Effects in Pd-YIG Hybrid Structures, Phys. Rev. Lett. **113**, 037203 (2014).
[15] Y. M. Lu, Y. Choi, C. M. Ortega, X. M. Cheng, J. W. Cai, S. Y. Huang, L. Sun, and C. L. Chien, Pt Magnetic Polarization on $Y_3Fe_5O_{12}$ and Magnetotransport Characteristics, Phys. Rev. Lett. **110**, 147207 (2013).
[16] S. Geprägs, S. Meyer, S. Altmannshofer, M. Opel, F. Wilhelm, A. Rogalev, R. Gross, and S. T. B. Goennenwein, Investigation of induced Pt magnetic polarization in $Pt/Y_3Fe_5O_{12}$ bilayers, Appl. Phys. Lett. **101**, 262407 (2012).
[17] T. Kuschel, C. Klewe, J. M. Schmalhorst, F. Bertram, O. Kuschel, T. Schemme, J. Wollschläger, S. Francoual, J. Strempfer, A. Gupta, M. Meinert, G. Götz, D. Meier, and G. Reiss, Static Magnetic Proximity Effect in $Pt/NiFe_2O_4$ and Pt/Fe Bilayers Investigated by X-ray Resonant Magnetic Reflectivity, Phys. Rev. Lett. **115**, 097401 (2015).
[18] K. Di, V. L. Zhang, H. S. Lim, S. C. Ng, M. H. Kuok, J. Yu, J. Yoon, X. Qiu, and H. Yang, Direct Observation of the Dzyaloshinskii-Moriya Interaction in a Pt/Co/Ni Film, Phys. Rev. Lett. **114**, 047201 (2015).
[19] Y. M. Lu, W. Cai, S. Y. Huang, D. Qu, B. F. Miao, and C. L. Chien, Hybrid magnetoresistance in the proximity of a ferromagnet, Phys. Rev. B **87**, 220409 (2013).
[20] M. B. Jungfleisch, V. Lauer, R. Neb, A. V. Chumak, and B. Hillebrands, Improvement of the yttrium iron garnet/platinum interface for spin pumping-based applications, Appl. Phys. Lett. **103**, 022411 (2013).
[21] Y. Y. Sun, Y. Y. Song, H. C. Chang, M. Kabatek, M. Jantz, W. Schneider, M. Z. Wu, H. Schultheiss, and A. Hoffmann, Growth and ferromagnetic resonance properties of nanometer-thick yttrium iron garnet films, Appl. Phys. Lett. **101**, 152405 (2012).
[22] A. Kehlberger, R. Röser, G. Jakob, U. Ritzmann, D. Hinzke, U. Nowak, M. C. Onbasli, D. H. Kim, C. A. Ross, M. B. Jungfleisch, B. Hillebrands, and M. Kläui, Length Scale of the Spin Seebeck Effect, Phys. Rev. Lett. **115**, 096602 (2015).
[23] S. Meyer, R. Schlitz, S. Geprägs, M. Opel, H. Huebl, R. Gross, and S. T. B. Goennenwein, Anomalous Hall effect in YIG/Pt bilayers, Appl. Phys. Lett. **106**, 132402 (2015).
[24] Y. Yang, B. Wu, K. Yao, S. Shannigrahi, B. Zong, and Y. Wu, Investigation of magnetic proximity effect in Ta/YIG bilayer Hall bar structure, J. Appl. Phys. **115**, 17C509 (2014).
[25] C. Tang, P. Sellappan, Y. Liu, Y. Xu, J. E. Garay, and J. Shi, Anomalous Hall hysteresis in $Tm_3Fe_5O_{12}/Pt$ with strain-induced perpendicular magnetic anisotropy, Phys. Rev. B **94**, 140403 (2016).
[26] J. H. Han, G. Y. Shi, X. J. Zhou, Q. H. Yang, Y. H. Rao, G. Li, H. W. Zhang, F. Pan, and C. Song, Vertical spin Hall magnetoresistance in $Ta_{1-x}Pt_x$/YIG bilayers, Phys. Rev. B **94**, 134406 (2016).
[27] X. Liang, Y. Zhu, B. Peng, L. Deng, J. Xie, H. Lu, M. Wu, and L. Bi, Influence of interface structure on magnetic proximity effect in $Pt/Y_3Fe_5O_{12}$ heterostructures, ACS Appl. Mater. Interfaces **8**, 8175 (2016).
[28] F. Grasset, S. Mornet, A. Demourgues, J. Portier, J. Bonnet, A. Vekris, and E. Duguet, Synthesis, magnetic properties, surface modification and cytotoxicity evaluation of $Y_3Fe_{5-x}Al_xO_{12}$ garnet submicron particles for biomedical applications, J. Magn. Magn. Mater. **234**, 409 (2001).
[29] J. P. Perdew, K. Burke, and M. Ernzerhof, Generalized Gradient Approximation Made Simple, Phys. Rev. Lett. **77**, 3865 (1996).
[30] J. P. Perdew, K. Burke, and M. Ernzerhof, ERRATA: Generalized Gradient Approximation Made Simple [Phys. Rev. Lett. 77, 3865 (1996)], Phys. Rev. Lett. **78**, 1396 (1997).
[31] P. E. Blöchl, Projector augmented-wave method, Phys. Rev. B **50**, 17953 (1994).
[32] G. Kresse and D. Joubert, From ultrasoft pseudopotentials to the projector augmented-wave method, Phys. Rev. B **59**, 1758 (1999).
[33] H. J. Monkhorst and J. D. Pack, Special points for Brillouin-zone integrations, Phys. Rev. B **13**, 5188 (1976).
[34] S. Dudarev, G. Botton, S. Savrasov, C. Humphreys, and A. Sutton, Electron-energy-loss spectra and the structural stability of nickel oxide: An LSDA+U study, Phys. Rev. B **57**, 1505 (1998).
[35] X. Guo, A. H. Tavakoli, S. Sutton, R. K. Kukkadapu, L. Qi, A. Lanzirotti, M. Newville, M. Asta, and A. Navrotsky, Cerium substitution in yttrium iron garnet: Valence state, structure, and energetics, Chem. Mater. **26**, 1133 (2014).
[36] F. Zhou, T. Maxisch, and G. Ceder, Configurational Electronic Entropy and the Phase Diagram of Mixed-Valence Oxides: The Case of Li_xFePO_4, Phys. Rev. Lett. **97**, 155704 (2006).
[37] N. J. Mosey, P. Liao, and E. A. Carter, Rotationally invariant ab initio evaluation of Coulomb and exchange parameters for DFT+U calculations, J. Chem. Phys. **129**, 014103 (2008).
[38] X. Zhou, L. Ma, Z. Shi, W. J. Fan, J. G. Zheng, R. F. L. Evans, and S. M. Zhou, Magnetotransport in metal/insulating-ferromagnet heterostructures: Spin Hall magnetoresistance or magnetic proximity effect, Phys. Rev. B **92**, 060402 (2015).
[39] F. Grasset, S. Mornet, A. Demourgues, J. Portier, J. Bonnet, A. Vekris, and E. Duguet, Synthesis, magnetic properties, surface modification and cytotoxicity evaluation of $Y_3Fe_{5-x}Al_xO_{12}$ ($0 \leq x \leq 2$) garnet submicron particles for biomedical applications, J. Magn. Magn. Mater. **23**, 409 (2001).
[40] H. A. Algra and P. Hansen, Temperature dependence of the saturation magnetization of ion-implanted YIG films, Appl. Phys. A **29**, 83 (1982).
[41] N. Nagaosa, J. Sinova, S. Onoda, A. H. MacDonald, and N. P. Ong, Anomalous Hall effect, Rev. Mod. Phys. **82**, 1539 (2010).
[42] Z. Wang, C. Tang, R. Sachs, Y. Barlas, and J. Shi, Proximity-induced Ferromagnetism in Graphene Revealed By the Anomalous Hall Effect, Phys. Rev. Lett. **114**, 016603 (2015).

[43] S. Meyer, M. Althammer, S. Geprägs, M. Opel, R. Gross, and S. T. Goennenwein, Temperature dependent spin transport properties of platinum inferred from spin Hall magnetoresistance measurements, Appl. Phys. Lett. **104**, 242411 (2014).

[44] Y. T. Chen, S. Takahashi, H. Nakayama, M. Althammer, S. T. Goennenwein, E. Saitoh, and G. E. Bauer, Theory of spin Hall magnetoresistance (SMR) and related phenomena, J. Phys. Conden. Matter **28**, 103004 (2016).